Heliyon 10 (2024) e25593

Contents lists available at ScienceDirect

Heliyon

journal homepage: www.cell.com/heliyon

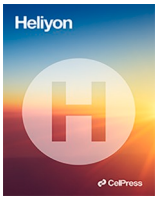

Research article

Effect of the molecular weight on the sensing mechanism in polyethylene glycol diacrylate/gold nanocomposite optical transducers

Bruno Miranda [a], Stefania Dello Iacono [b,*], Ilaria Rea [a], Fabio Borbone [c], Luca De Stefano [a]

[a] Institute of Applied Sciences and Intelligent Systems (ISASI), National Research Council, Via P. Castellino 111, Naples, 80131, Italy
[b] Institute of Polymers, Composites and Biomaterials (IPCB), National Research Council, P.le Enrico Fermi 1, 80055, Portici, Italy
[c] Department of Chemical Sciences, University of Naples "Federico II", Complesso Universitario di Monte Sant'Angelo, Via Cintia 21, Naples, 80126, Italy

ARTICLE INFO

Keywords:
Polyethylene glycol diacrylate
Gold nanoparticles
Nanocomposites
Biosensing
Plasmonics
Hydrogels
Polymers
Optical transducers

ABSTRACT

The combination of plasmonic nanoparticles and hydrogels results in nanocomposite materials with unprecedented properties that give rise to powerful platforms for optical biosensing. Herein, we propose a physicochemical characterization of plasmonic hydrogel nanocomposites made of polyethylene glycol diacrylate (PEGDA) hydrogels with increasing molecular weights (700–10000 Da) and gold nanoparticles (AuNPs, ~60 nm). The swelling capability, mechanical properties, and thermal responses of the nanocomposites are analyzed and the combination with the resulting optical properties is elucidated. The different optomechanical properties of the proposed nanocomposites result in different transduction mechanisms, which can be exploited for several biosensing applications. A correlation between the polymer molecular weight, the effective refractive index of the material, and the optical response is found by combining experimental data and numerical simulations. In particular, the localized surface plasmon resonance (LSPR) position of the AuNPs was found to follow a parabolic profile as a function of the monomer molecular weight (MW), while its absorbance intensity was found as inversely proportional to the monomer MW. Low MW PEGDA nanocomposites were found to be responsive to refractive index variations for small molecule sensing. Differently, high MW PEGDA nanocomposites exhibited absorbance intensity increase/decrease as a function of the hydrophobicity/hydrophilicity of the targeted small molecule. The proposed optomechanical model paves the way to the design of innovative platforms for real-life applications, such as wearable sensing, point-of-care testing, and food monitoring *via* smart packaging devices.

1. Introduction

In the last decades, low-cost, versatile, and large-scale optical biosensors have become in great demand. Biosensors are expected to overcome the current limitations of traditional remote laboratory techniques, which include the need for trained personnel, expensive instrumentation, and long waiting times. Such long times are not compatible anymore with the maintenance of human health, food

* Corresponding author.
E-mail address: stefania.delloiacono@cnr.it (S. Dello Iacono).

https://doi.org/10.1016/j.heliyon.2024.e25593
Received 21 November 2023; Received in revised form 29 January 2024; Accepted 30 January 2024
Available online 5 February 2024

quality assessment, and environmental monitoring [1–7].

Therefore, the investigation of novel hybrid materials, starting from well-known isolated components, is pushing researchers toward a multidisciplinary approach including materials science, physics, engineering, and life sciences [8–11]. In this context, metallic nanoparticles (NPs) with unique optical features and polymers with intrinsic mechanical properties are emerging as promising candidates. The main aim is the design of flexible optical devices. The advantages of such devices are ease of integration into complex systems, adaptability to non-planar substrates, deformability, and simplicity of sample collection [12].

Specifically, noble metal NPs exhibit LSPR in the visible and near-infrared regions of the spectrum (400–900 nm) [13]. The strong electromagnetic field enhancement in their surroundings enables high-resolution chemical sensing in both label-free and non-label-free modes [13,14]. Furthermore, plasmonic NPs have emerged for their simple fabrication *via* both top-down and bottom-up strategies and characterization with rapid spectroscopic strategies. Despite plasmonic NPs being generally assembled onto rigid substrates, such as silicon, glass, or quartz, there is a new tendency to obtain similar analytical performances on/within polymeric substrates, *e.g.,* polydimethylsiloxane (PDMS), polymethylmethacrylate (PMMA), and so on [15–18].

More recently, a new class of polymers obtained from the crosslinking of hydrophilic polymer chains, namely hydrogels, is finding large applications in the biosensing field. Hydrogels can absorb large amounts of water, even in response to different *stimuli*. Their mechanical properties can be opportunely engineered to achieve bio-responsive materials that can be applied directly *in situ* to monitor chemical analytes, physiological parameters, and environmental pollutants [19–22]. Moreover, they generally exhibit optical transparency, which is fundamental for preserving and isolating the optical properties of plasmonic NPs.

The powerful combination of hydrogels with plasmonic NPs has been already assessed and reported by several groups. For example, hydrogels, due to their swelling capability, can be used to enhance the optical response of a plasmonic substrate to refractive index variations, as reported by Mesch et al. [23]. Briefly, their results are based on the photocuring of a hydrogel thin layer on top of a plasmonic nanoantenna. On the contrary, nanocomposite hydrogels are self-standing platforms obtained by the gentle mixing of plasmonic NPs to the pre-polymer solution of monomers, which are then cured by thermal or optical crosslinking [24]. With this fabrication approach, it is possible to obtain hybrid materials combining the optical features of the plasmonic NPs and the mechanical properties of hydrogels. For example, AuNPs can be embedded within thermoresponsive hydrogels, thus obtaining a colorimetric biosensor capable of measuring body temperature with good sensitivity, as reported by Choe et al. [25].

Therefore, hydrogel nanocomposites enable novel functionalities starting from the absorption variations due to the swelling of the polymeric matrix. In our previous studies, we obtained two different optical transducers based on PEGDA hydrogels and spherical AuNPs [26–28]. PEGDA possesses a simple molecular structure and is highly transparent. We showed that it is an excellent matrix for the embedding and stabilization of AuNPs and that it exhibits high chemical and mechanical stability [26,27].

However, when dealing with novel hybrid materials, a systematic characterization of their physicochemical properties can be of paramount importance for a comprehensive understanding of the potential application of the device in the field of interest [29]. Even though the physical and chemical properties of the single materials have been already reported [30,31], a proper characterization of their combination is still missing.

Therefore, in the present study, PEGDA/AuNPs nanocomposite thin films based on four different PEGDA are presented. The pre-polymer solutions consist of PEGDA monomers with different MWs (700, 2000, 6000, and 10,000 Da, respectively). The obtained nanocomposites are characterized by absorption spectroscopy, spectroscopic ellipsometry (SE), scanning electron microscopy (SEM), dynamic mechanical analysis (DMA), Fourier Transform infrared spectroscopy (FTIR), thermogravimetric analysis (TGA), differential scanning calorimetry (DSC), and equilibrium water content (EWC). Starting from the obtained experimental values, we elucidate the effect of the MW of the four polymeric matrices on the optical responses of the AuNPs embedded within them. The results are supported by numerical simulations. The proposed study offers new insights into the use of PEGDA/AuNPs hydrogel nanocomposites in biosensing applications, guiding the readers through the choice of the most appropriate combination of the two materials to achieve the desired analytical performances.

2. Materials and methods

2.1. Materials

Tetrachloroauric acid ($HAuCl_4$), trisodium citrate ($Na_3C_6H_5O_7$), poly(ethylene glycol) diacrylate (PEGDA, average Mn 700), poly (ethylene glycol) diacrylate (PEGDA, average Mn 2000), poly(ethylene glycol) diacrylate (PEGDA, average Mn 6000), poly(ethylene glycol) diacrylate (PEGDA, average Mn 10,000), 2-hydroxy-2-methylpropiophenone (Darocur 1173), and cysteamine were purchased from Merck KGaA (DE).

2.2. Synthesis of gold nanoparticles (AuNPs)

Spherical AuNPs with a size of 60 ± 20 nm were chemically synthesized by a seed-mediated growth, by adapting the protocol reported in Ref. [30]. Briefly, a trisodium citrate solution (2.2 mM, 150 mL) was heated up to 100 °C under vigorous stirring. $HAuCl_4$ (1 mL, 25 mM) was suddenly added to the boiling solution. After about 10 min, Au seeds (~10 nm, 3×10^{12} NPs mL^{-1}) were obtained, as confirmed by the deep variation to red color. Afterward, the seed solution was cooled to 90 °C. At this stage, two injections of $HAuCl_4$ solution (1 mL, 25 mM) were performed as a first growth step. A reaction time of 30 min was established for each injection. After 1 h, part (55 mL) of the solution was removed and the remaining was diluted with Milli-Q water (53 mL) and trisodium citrate solution (2 mL, 60 mM). The diluted solution was used for the subsequent growth step. The size of the AuNPs was monitored up to 60

nm by Dynamic Light Scattering (DLS). The synthesis proceeded until the eighth growth step, corresponding to nanoparticles of 60 ± 20 nm ($PDI = 0.11 \pm 0.02$). UV-Vis spectra of the freshly synthesized AuNPs were also collected. The DLS measurements were performed using Zetasizer Nano ZS (Malvern Instruments, UK) equipped with a HeNe laser (633 nm, fixed scattering angle of 173°, 25 °C), while UV–Vis absorbance spectra were measured using Cary 100 spectrometer (VARIAN), from 250 to 900 nm.

2.3. Preparation of PEGDA/AuNPs nanocomposites

The freshly synthesized AuNPs (250 μg/mL) were concentrated (10 ×) by centrifugation at 1920*g* at 10 °C for 10 min. The pre-polymer solutions of PEGDA with increasing MWs were obtained by fixing the concentration of PEGDA, the amount of photo-initiator (PI), and AuNPs embedded within all the pre-polymer solutions to achieve comparable nanocomposites. The final composition of the four prepolymer solutions object of this study is summarized in Table 1. The monomers were dissolved in water to obtain the desired concentrations (400 mg/mL) and sonicated for 10 min until complete dissolution. Then, Darocur 1173, acting as a PI, was mixed with the polymeric solutions under magnetic stirring for 5 min up to a final weight fraction of 10 %. Finally, concentrated AuNPs were gently added to the four different solutions. The crosslinking of the four different nanocomposites was performed by enclosing the abovementioned pre-polymer solutions (270 μL of solution for each film) between two coverslips (24 × 24 mm^2) and photo-polymerizing them by UV-light at 365 nm for 5 min in a UV-exposure box (UV-Belichtungsgerät 2). Thin films of hydrogel nanocomposite (thickness of ~400 μm) having the typical coloration of colloidal AuNPs were finally obtained (Fig. S1). For the mechanical elongation tests, the same pre-polymer solutions were prepared and cured into a glass mold to achieve a uniform rectangular shape (6 mm × 24 mm) and a thickness below 1 mm. For the optical characterizations, SEM imaging, and swelling measurements, instead, the 24 × 24 mm^2 thin films were cut into disks (7 mm diameter) using a puncher to guarantee uniform functional area and volume to be tested. To have a white reference, the same pre-polymer solutions, without AuNPs, were photo-polymerized in the same conditions. The functionalization of the disk nanocomposites with cysteamine was performed by soaking them into cysteamine water solutions with concentrations ranging from 50 μM to 2.0 mM. The sensitivity S of the four different optical transducers was evaluated by considering the slope of the linear regions in the calibration curves reported in Fig. 8a and b, where possible (Table S2). The Limits of Detection (LODs) where computed according to equation (1):

$$LOD = \frac{3\sigma}{S} \tag{1}$$

where σ here denotes the SD of the measurements performed on the bare samples (without cysteamine).

2.4. Swelling properties

The swelling experiments were carried out by immersing circular thin films, 7 mm in diameter, previously dried in an oven (40 °C, overnight) and weighted, in Milli-Q water at room temperature. The composite specimens were periodically taken out of the water, dabbed with paper to remove excess surface water, and weighted until no more changes were recorded. Swelling ratio (SR) values are the average of measurements performed in triplicate, calculated according to Equation (2):

$$SR = (W_t - W_0) / W_0 \tag{2}$$

where W_t is the weight of the sample at time t and W_0 is the weight of the dry specimen.

2.5. Optical characterization

The thin hydrogel nanocomposites obtained starting from the pre-polymer solutions summarized in Table 1 were characterized using the customized transmission mode setup at normal incidence reported in Refs. [26,27]. Briefly, a halogen light source was used as the excitation to measure the plasmonic absorbance in the desired wavelength range (400–900 nm). The light was guided by a Thorlabs fiber reaching a collimator on the top of each sample. The transmitted light was finally conveyed by another Thorlabs fiber to a spectrometer (Filmetrics). A schematic representation of the optical setup is reported in Fig. S1. All the spectra were collected in the range of 400–900 nm with a resolution of ≈0.35 nm. The raw absorption spectra were smoothed to remove noise by using adjacent average filtering and the peak analysis and absorption intensity evaluations were performed in Origin. Before each measurement, the excess water was removed to minimize light scattering and noise. The size of the collimated light spot conveyed on the samples and the distance between the two optical fibers were kept constant for all the measurements to guarantee the collection of comparable signals

Table 1
Composition of the pre-polymer solutions.

Sample	PEGDA MW (Da)	Polymer Mass (mg)	PI Fraction % (w/w)	NPs Fraction % (w/w)	Total Volume (μL)
P700Au	700	108	10	0.3	270
P2000Au	2000	108	10	0.3	270
P6000Au	6000	108	10	0.3	270
P10000Au	10,000	108	10	0.3	270

and significant statistics.

2.6. Spectroscopic ellipsometry

Variable angle spectroscopic ellipsometry measurements (UVISEL, Horiba, Jobin–Yvon) were performed on thin hydrogel films left to dry on silicon substrates. The thin films of the four different PEGDA were prepared by using the same ratios reported in Table 1, except for AuNPs - here absent. One of the two coverslips was replaced with a silicon wafer, and 3 μ L of the solutions were drop-cast on the silicon wafer and squeezed to achieve thin films of thickness below 1 μ m. The spectra were recorded in the spectral range of 300–1600 nm. The refractive index was then reported only in the range of 400–900 to be consistent with the other recorded spectra. The measurements were performed at five different incident angles (50°, 55°, 60°, 65°, and 70°). The Sellmeier transparent model was used [32], according to Equations (3) and (4):

$$n^2(\lambda) = A + \frac{B\lambda^2}{\lambda^2 - {\lambda_0}^2} \tag{3}$$

$$k(\lambda) = 0 \tag{4}$$

where n is the real part of the refractive index and k is the imaginary part of the refractive index, generally associated with materials' intrinsic absorption and, therefore, set to 0, as imposed from the Sellmeier transparent model. A, B, and λ_0 are empirical parameters that are derived from the fitting of the measured dispersion curves.

2.7. Scanning electron microscopy

Freeze-drying of the hydrogel nanocomposites was carried out before their SEM imaging. This process allowed the preservation of the microstructure of the nanocomposites in their swollen state, even after the water removal [31]. Briefly, the hydrogel disks embedding AuNPs were swollen in Milli-Q water for 24 h and put in liquid nitrogen until complete freezing of the samples. Rapidly, they were set in a freeze dryer overnight, at − 40 °C, and under vacuum to allow the complete sublimation of the water inside the networks. The freeze-dried samples were finally mounted on carbon tape and sputtered with a layer of Au/Pd using a Denton Vacuum Desk V TSC coating system before observation. SEM images were acquired with a field-emission gun (FEG–SEM) FEI/ThermoFisher Nova NanoSEM 450 microscope. The estimation of the mesh pore size was performed by using the ImageJ software by performing a particle analysis on the detected contour lines after converting the images into binary bitmaps.

2.8. Fourier transform infrared spectroscopy

FTIR spectra of nanocomposite PEGDA-based and relative monomers were recorded at 25 °C and 1 atm by a Perkin Elmer Frontier spectrometer, coupled with an attenuated total reflectance (ATR) accessory, where a diamond crystal with the angle of incidence for the IR beam of 45° is used. Each spectrum is the average of 64 acquisitions in the wavenumber range from 4000 cm^{-1}–650 cm^{-1}, with a wavenumber resolution of 4 cm^{-1}. ATR and linear baseline corrections have been applied to remove the effect of the collection mode (reflectance) and baseline fluctuation on the spectra, respectively.

2.9. Calorimetric characterization

Thermogravimetric analysis was carried out in an inert atmosphere (dry nitrogen with a flow rate of 10 mL/min), using a TA Instrument Q5000. The samples were previously dried in an oven (40 °C, overnight) to eliminate the fabrication water content and any light volatile matter present. The mass loss was determined by heating the dried samples from 35 to 600 °C with a temperature ramp of 10 °C/min.

Differential scanning calorimetry was performed by the TA Instrument Discovery calorimeter. For each film, approximately 5 mg of dried sample was sealed into a Tzero pan with a hermetic Tzero lid. Three temperature scans were consecutively carried out in N_2 purge (rate of 50 mL/min) with a controlled ramp of 10 °C/min, in both heating and cooling modes. The samples, previously cooled at −85 °C, were first heated to 180 °C, then cooled to −85 °C, and finally heated again to 180 °C. TA TRIOS software was used to analyze the DSC thermograms.

2.10. Mechanical characterization

Uniaxial tensile tests were carried out on thin strips, with nominal size 24.0 x 6.0 × 1.0 mm^3, using a DMA Q800 (TA Instruments, USA). The samples, after the removal of excess water, were grabbed between the wedges and stretched at a constant displacement rate of 0.50 mm min^{-1}. All experiments were performed at 25 °C and 1 atm, at least on 5 different specimens for each nanocomposite film.

2.11. Numerical simulations

Numerical simulations were performed in the framework of the Mie Theory, which first provided the analytical solution to the

scattering problem of a single sphere of radius *r* starting from Maxwell equations [33–36]. Being the AuNPs stabilized with trisodium citrate, they were assumed as hybrid NPs [26,27,37]. Therefore, each AuNP was modeled as a sphere made of two main components, namely gold, and citrate. Citrate inclusions were modeled as a Gaussian distribution of spheres within the AuNP, with mean volume fraction μ and standard deviation σ. Starting from the knowledge of gold and citrate permittivities, and from the measured absorption spectra, μ and σ were obtained through genetic algorithm (GA) optimization [34,38]. The fitness function to be minimized F (μ, σ) was the root mean square of the difference between theoretical and experimental data, as reported in Equation (5):

$$F(\mu,\sigma) = \left\| C_{abs_{th}}\left(\lambda, \varepsilon_{eff}(\mu,\sigma)\right) - C_{abs_{exp}}(\lambda) \right\| \tag{5}$$

where $C_{abs_{th}}$ is the theoretical absorption cross-section as a function of the effective dielectric permittivity of the hybrid AuNP (ε_{eff}) and $C_{abs_{exp}}$ is the measured absorbance of AuNPs in water ($n_{Water} = 1.333$). The effective dielectric permittivity of the hybrid AuNP was obtained by the Maxwell-Garnett homogenization theory by using the experimental constants derived by Johnson and Christie for gold [39] and the citrate refractive indices ($n_{Citrate} = 1.39$) [40,41]. The theoretical spectrum of the AuNPs ($C_{abs_{th}}$) was predicted analytically by the Mie Theory. The radius of AuNP was set to 30 nm, in agreement with the particle analysis carried out by DLS measurements. The GA fitness value was set to 0.1, corresponding to a 10 % deviation between theory and experiments. Once the difference between theory and experiments was found for AuNPs in solution, the effective refractive index of the surrounding medium $n_{eff.m}$ was estimated starting from the PEGDA refractive index measured by SE and the water content, derived from SR measurements. A correlation between the predicted LSPR position and intensity was found as a function of the PEGDA MW, as reported in the Results and Discussion section. Finally, the prediction of the LSPR position and intensity was performed by considering the formation of a monolayer of cysteamine on the free portion of the AuNP surface ($n_{Cys} = 1.74$). The model enables the accurate fitting of the experimental data as a function of the cysteamine concentration, in all the nanocomposites, namely P700Au, P2000Au, P6000Au, and P10000Au.

3. Results and discussion

In this work, we report on the physicochemical properties of PEGDA/AuNPs nanocomposites for biosensing applications. For the first time to our knowledge, we unravel the influence of the PEGDA MW on the optical properties of the AuNPs embedded within the hydrogel matrix.

Starting from the optical, chemical, and mechanical properties of four different networks polymerized in the same conditions and embedding AuNPs (~60 nm) in the same concentration (see Fig. 1 and Table 1), we derived the theoretical prediction of the effective refractive index of the medium in which the AuNPs are immersed. The obtained model directly finds applications in the biosensing field, since, according to the initial LSPR response, the evolution of the absorbance peaks can be followed and predicted both in position and/or in intensity according to the selected monomer MW.

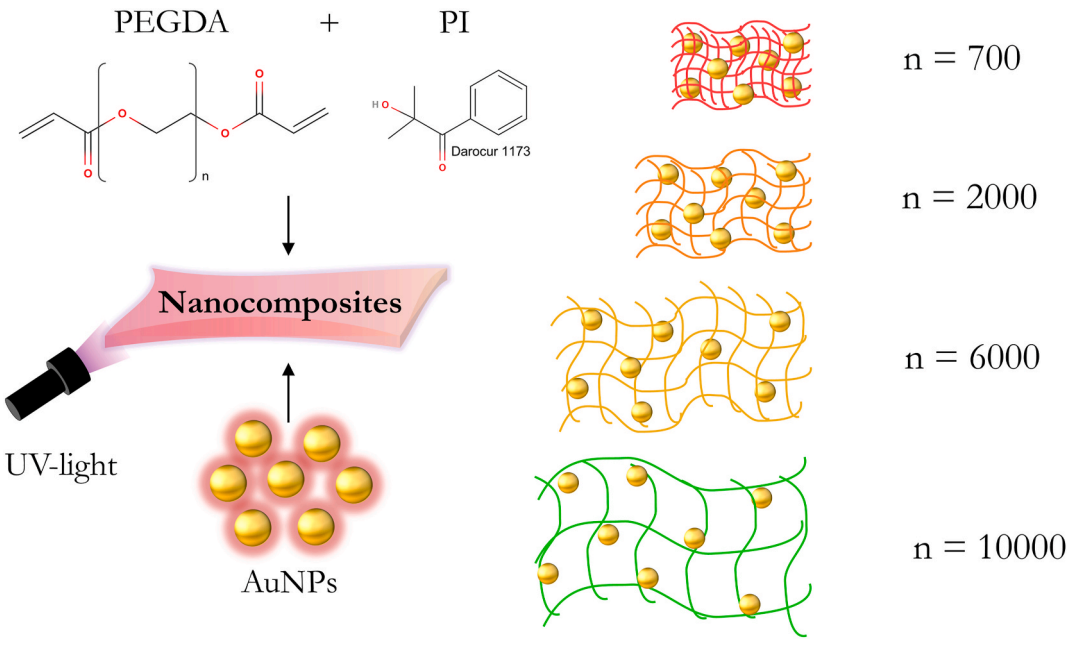

Fig. 1. a) Fabrication scheme of PEGDA (n = 700, 2000, 6000, 10,000)/Au NPs thin films by radical photopolymerization.

3.1. Optical properties of unloaded PEGDA hydrogel thin films

A good polymeric substrate for 3D plasmonic transducers must have good optical transparency to investigate the optical properties of the NPs embedded within it and known optical constants (refractive index) to allow the theoretical fitting of the plasmonic response [12,42].

Therefore, the transmission spectra of PEGDA hydrogel thin films were collected by customized transmission optical setup (Fig. S1), as described in the experimental section. We set the swelling time at 24 h, as reported in the experimental section. This choice was made to be sure that all the samples had reached their equilibrium. As shown in Fig. 2a, all the PEGDA hydrogels exhibit excellent transparency between 550 and 900 nm. The optical transparency undergoes a slight decrease in the range of 400–550 nm, as it generally happens for all organic compounds. However, all the selected hydrogels can be considered sufficiently transparent to monitor the optical signal of a suitable density of plasmonic NPs. Moreover, when performing absorbance measurements in the transmission mode, the background coming from the substrate is generally subtracted. The background correction was performed using the unloaded (without NPs) hydrogel as a reference standard.

While the refractive indexes of the PEGDA monomers generally come with their datasheet, the refractive indexes of the polymerized hydrogels dried on silicon were measured by SE, as reported in the experimental section. The obtained results are shown in Fig. 2b. A slight increase in the refractive index n as a function of the hydrogel MW can be observed. More precisely, PEGDA 700 and 2000 (red and orange curves) show similar behavior in the NIR, while a significant difference is recorded in the Vis range, where PEGDA 2000 shows a higher refractive index. A further increase in the refractive indexes can be observed for PEGDA 6000 and 10,000 (yellow and green curves). All the polymerized versions of PEGDA exhibited a higher refractive index with respect to their monomer counterparts [43,44].

This significant difference may be attributed to the formation of the polymerized network operated by the PI, which makes the hydrogel network denser and more viscous than the unpolymerized monomers.

3.2. Morphological characterization

The morphological characterization of the four nanocomposites object of this study was performed by SEM imaging to i) visualize the microstructure of the hydrogel network, ii) derive information on the network pore size distribution as a function of the MW, iii) visualize the distribution of the AuNPs within the hydrogel, iv) gather information on the physicochemical stability of the AuNPs within the polymeric matrix.

To preserve the architecture of the nanocomposites before SEM, we carried out a freeze-drying process of the obtained hydrogel disks (Sections 2.3 and 2.7). The results of the SEM characterization are summarized in Fig. 3a and b. At lower magnifications (8000×), in Fig. 3a, the surface morphology appears compact and uniform for P700Au and becomes progressively rougher and more inhomogeneous with increasing MW (in the case of P2000Au) until it shows an obvious sponge-like structure in the case of P6000Au and P10000Au. At higher magnifications (50,000×), in Fig. 3b, rather homogeneous distribution of AuNPs on the surface of the hydrogels and no clustering are observed for all the samples.

The estimation of the pore sizes of the hydrogel nanocomposites was performed by ImageJ software (Fig. 3c). As expected, the network mesh size was found to increase as a function of the hydrogel MW. More precisely, in the fully swollen state, the network mesh size of P700Au was $0.5 \pm 0.3\ \mu m$, which increased to $1.6 \pm 0.9\ \mu m$, $8 \pm 3\ \mu m$, and $20 \pm 7\ \mu m$, in the case of P2000Au, P6000Au, and P10000Au, respectively. The AuNPs within all the polymeric networks preserved their shape and size distribution. On average, the AuNPs were found well-dispersed into the networks and with dimensions falling in the same range of DLS measurements. In particular,

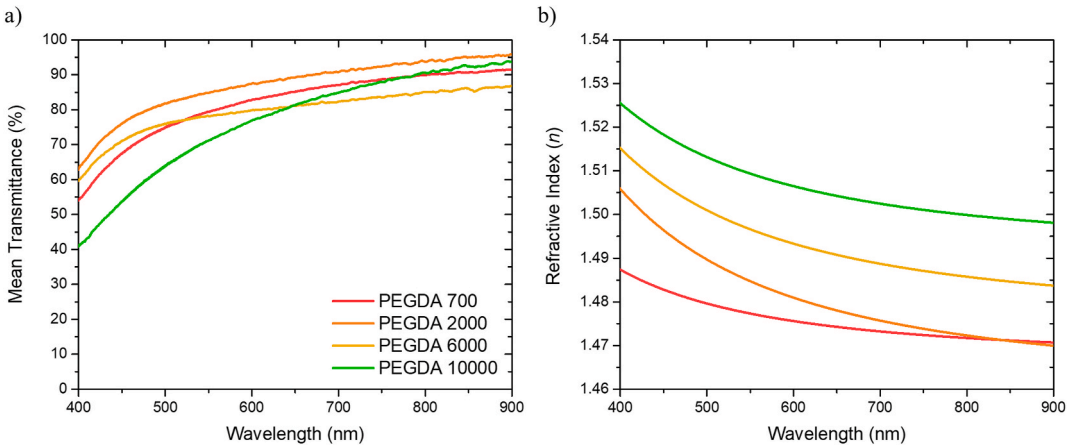

Fig. 2. a) Mean transmittance (%) of PEGDA (700, 2000, 6000, 10,000) hydrogel thin films for the estimation of the optical transparency in the Vis-NIR spectrum (400–900 nm) ($n \geq 3$). b) Refractive index (n) of PEGDA (700, 2000, 6000, 10,000) hydrogel thin films obtained from SE measurements.

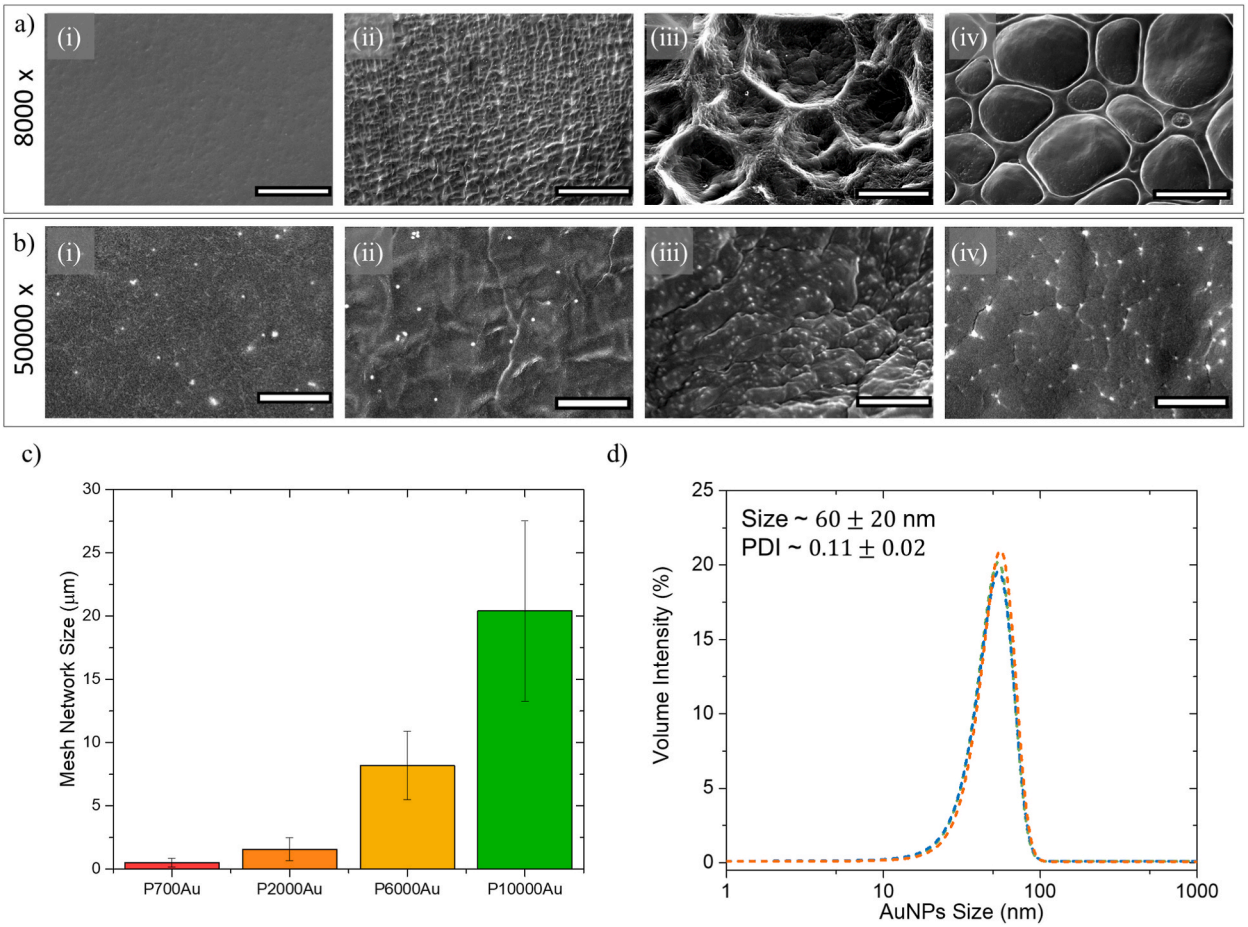

Fig. 3. a) SEM images of freeze-dried P700Au, P2000Au, P6000Au, and P10000Au samples (i-iv, respectively) at a magnification of ~ 8000× (scale bar is 10 μ m) to observe the microstructure of the hydrogel with increasing MW. b) SEM images of freeze-dried P700Au, P2000Au, P6000Au, and P10000Au samples (i-iv, respectively) at a magnification of ~ 50000× (scale bar is 2 μ m) to observe the distribution of AuNPs within the hydrogel networks. c) Barplot of the average (±*SD*) mesh network size as a function of the PEGDA MW (extrapolated from SEM images at lower magnitude). d) synthesized AuNPs size distribution evaluated by DLS measurements (before their embedding in the hydrogel network).

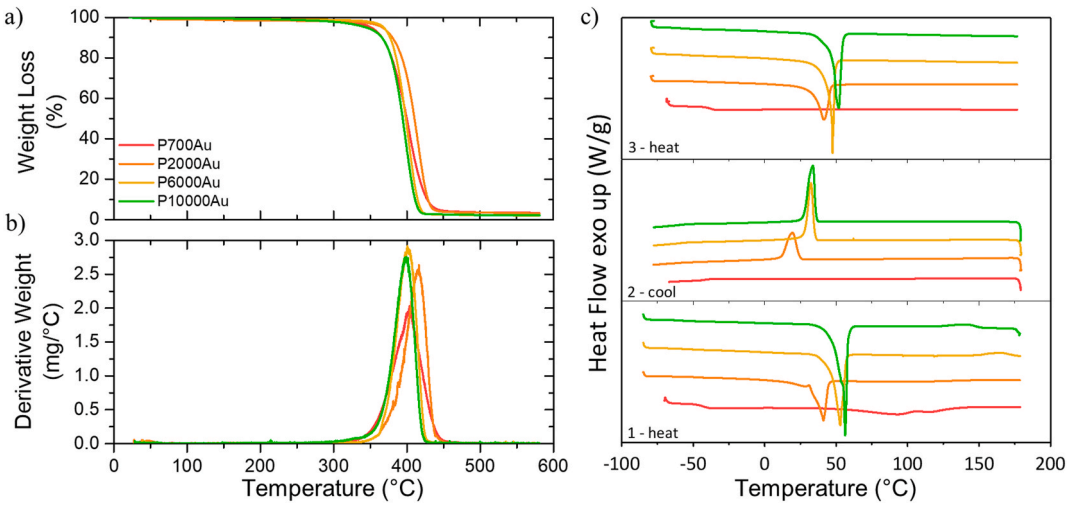

Fig. 4. (a) Thermogravimetric curves of dried P700Au, P2000Au, P6000Au, and P10000Au. (b) Derivative thermograms of dried P700Au, P2000Au, P6000Au, and P10000Au. (C) DSC thermograms of the dried PEGDA-based nanocomposites.

the AuNPs involved in this study exhibited a hydrodynamic radius of 60 ± 20 nm with good monodispersity (PDI = 0.11± 0.02) before their embedding in the polymeric network (Fig. 3d). Overall, the AuNPs with the four nanocomposites are dispersed enough to be assumed as *non-interacting* in the numerical simulations.

3.3. Thermal and spectroscopic analysis

The thermal stability of the nanocomposite PEGDA-based films was evaluated by recording the degradation *via* thermogravimetric analysis (TGA) and derivative thermogravimetry (DTG). For all MWs, the 5 % weight loss temperature, which is herein considered as the onset of degradation, was more than 350 °C, showing remarkable thermal stability over a wide operating range. A closer examination of the TGA and DTG thermograms, reported in Fig. 4a and b, respectively, reveals that the PEGDA/AuNPs nanocomposites were thermally degraded in a single decomposition stage, indicating the absence of chemisorbed water, namely lattice water, in dried samples. The greater thermal stability for small PEGDA MWs, evident in derivative thermograms (Fig. 4b), is due to their higher crosslinking grade. Additional covalent bonds require higher temperatures to break, thus slightly inhibiting the degradation process. However, for all the nanocomposite films, the degradation, consisting of 96.7–98.0 % weight loss within the 350−430 °C temperature range under pyrolysis conditions, resulted in a residue – char and NPs - of 2.0–3.3 %.

Fig. 4c shows PEGDA-based nanocomposite DSC thermograms, with various MWs. Regardless of the MW of the respective monomers, the first heating scan from −85 °C to 150 °C exhibited a complete degree of polymerization. There was no residual crosslink enthalpy that could support the exothermic process (cleavage of a π-bond and generation of a σ one) in case of radical reaction events. For higher MWs (2000, 6000, and 10,000), due to the long linear polymer chains, the melting temperature (T_m) and crystallization (T_c) are evident in heating and cooling scans respectively. T_m and T_c increase with MW, while the glass transition temperature (T_g) decreases exponentially as a function of the MW (Fig. S2).

FTIR spectroscopy is an efficient tool for non-destructively evaluating material properties. In detail, ATR spectra of monomers and relative polymer-based nanocomposites were compared in Fig. 5 to determine the polymerization degree rapidly. Spectra were normalized by the absorbance of C=O stretching at 1730 cm^{-1}, whose intensity does not change during the curing, while the position is slightly shifted, probably due to variation in network density and the presence of AuNPs. The crosslinking process was ascertained by monitoring the change in intensity of the bonds' peaks involved in the network formation. A decrease in the transmittance of the C=C stretching at ~1635 cm^{-1}, due to the cleavage of the group (-CH=CH_2) to form the new bond, was observed. Analogously, the bands located at 990 cm^{-1} and at 810 cm^{-1}, and 1410 cm^{-1}, relating to stretching and twisting vibrations of =C-H, and scissoring of =CH_2 in the monosubstituted vinyl group, respectively, reduced in intensity. The monitoring of the peaks (Fig. 5), susceptible to change with the progress of polymerization, demonstrated a complete reaction of all PEGDA monomers, aside from the respective MWs. However, it is noteworthy that variations are more evident for PEGDA 700, since the lower the monomer MW, the more numerous the functional groups involved in the crosslinking reaction at equal mass are.

3.4. Mechanical characterization

Fig. 6 shows the storage modulus (E), the elongation at the break (ε_b), and the swelling ratio (SR) of PEGDA-based nanocomposites obtained from monomers of increasing MW, hence the interesting correlation between these properties.

Young's modulus was found to be sensitive to the MW. As shown in Fig. 6a, it decreases with the increase of MW, varying from 1.91 ± 0.41 MPa for P700Au to 0.10 ± 0.02 MPa for P10000Au. These results are due to the lower crosslinking density and subsequent

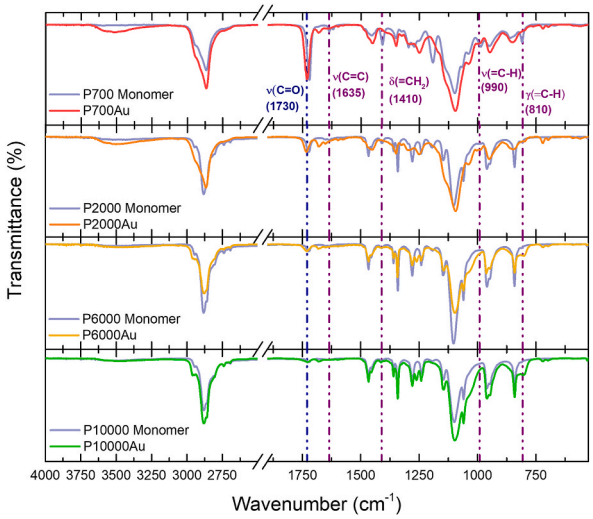

Fig. 5. ATR FTIR spectra of P700Au, P2000Au, P6000Au, and P10000Au nanocomposites and their monomers in direct comparisons.

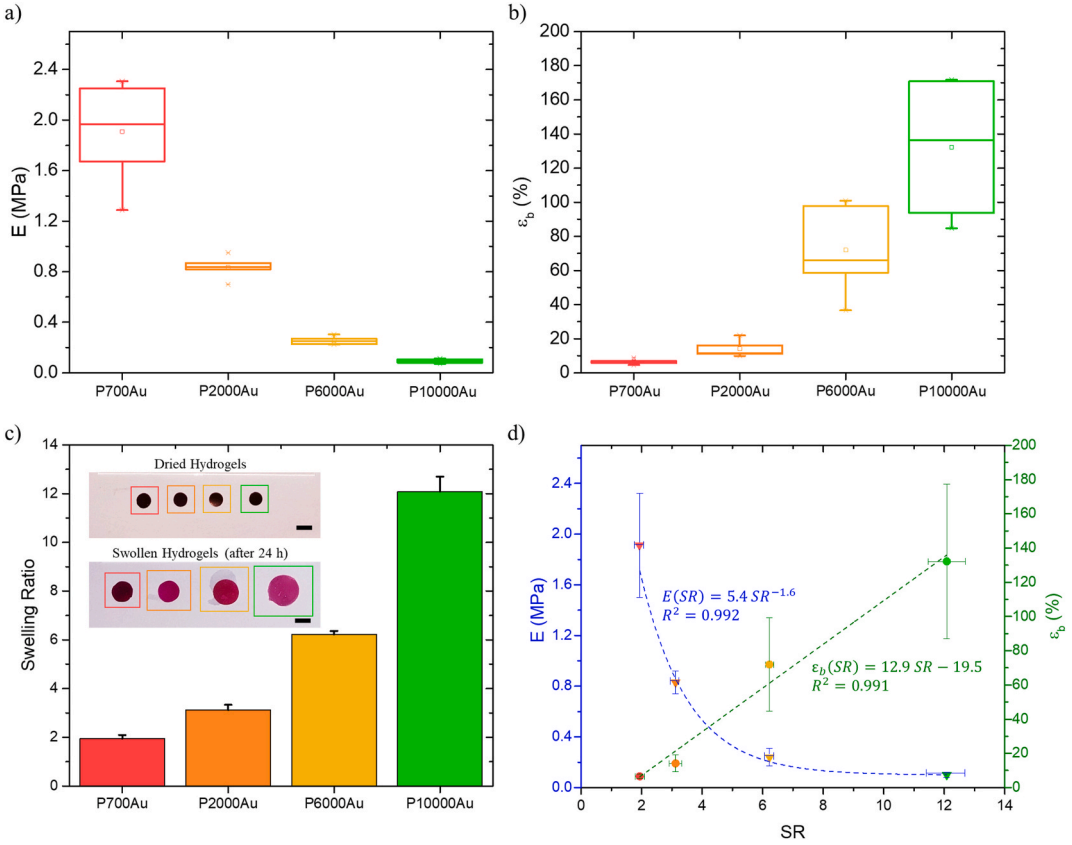

Fig. 6. (a) Scar plot of the E (MPa) of P700Au, P2000Au, P6000Au, and P10000Au after tensile tests ($n \geq 5$). (b) Scar plot of the ε_b (%) of P700Au, P2000Au, P6000Au, and P10000Au after tensile tests ($n \geq 5$). (c) SR of P700Au, P2000Au, P6000Au, P10000Au after 24 h swelling in Milli-Q water ($n \geq 3$). In the inset, digital photographs of dried (on the top) and swollen (on the bottom) P700Au, P2000Au, P6000Au, P10000Au (from left to right) hydrogel nanocomposite disks and after 24 h of swelling in Milli-Q water. Scale bars are 5 mm. (d) Mechanical properties - E (MPa, triangle) and ε_b (%, square) - of P700Au, P2000Au, P6000Au, and P10000Au as a function of relating SR.

higher water content and chain mobility that forbid energy storage in composites with higher MW.

As expected, there was a direct correlation also between elongation at break and MW. The data collected by tensile tests in Fig. 6b show that the stretching ability gradually decreases with the reduction in the MW of the monomer. The observed evolution, from 130.2 ± 45.1 % for P10000Au to 6.5 ± 1.4 % for P700Au, is ascribable to higher static stiffness, resulting in hindered chain mobility, in the case of lower MW.

Furthermore, the SR was evaluated since it is an important parameter of hydrogels that strongly affects mechanical properties. Measurements data in Fig. 6c reported a clear relationship between SR and molecular weight, coupled with isotropic variations in sizes and volume (Fig. 6c, inset). Hence, the above mechanical properties have been reported as a function of the swelling ratio, to highlight the direct correlation between molecular structure and swelling capability, and the subsequent relationship with the mechanical characteristics. In detail, the elongation at break linearly depends on the SR (Fig. 6d, square symbol), with a very good correlation coefficient (*i.e.,* the square of the correlation coefficient, $R^2 = 0.99$).

Similarly, the elasticity (Fig. 6d, triangle symbol) resulted in relation to the SR *via* a power-law fitting curve into the low-swelling (or Gaussian) regime, *i.e.,* SR < 20, with an equally excellent accord ($R^2 = 0.99$), as reported in equation (6).

$$E \propto SR^b \tag{6}$$

with b = −1.6.

In light of the good compliance, the found relationships could be applied to predeterminate the values of elongation at break or storage modulus when SR is known. Thus, they could be used in modeling theoretical and practical experiments for designed tunable materials.

3.5. Optical characterization and theoretical modeling

In the previous sections, the chemical and mechanical properties of the proposed hydrogel nanocomposites were characterized and

elucidated. PEGDA/AuNPs nanocomposites have been already demonstrated as promising transducers for biosensing applications [26, 27]. However, a theoretical study on how the monomer MW affects the optical properties of the final nanocomposite and the sensing mechanism was still missing.

Therefore, based on the physicochemical properties of the nanocomposites, a correlation between the LSPR position and intensity of the AuNPs embedded within PEGDA with different MW was found.

First, the experimental absorbance of the thin film nanocomposites was measured in transmission mode. The light spot and the distance between the two optical fibers were kept constants for all the measurements. The results of the optical characterization are shown in Fig. 7a. The mean absorbance spectra of the nanocomposites at the swelling equilibrium are reported as continuous lines, while confidence intervals are reported as dashed lines. The typical optical response of AuNPs is clearly observable. Moreover, due to the all-solution fabrication strategy, the optical response of the nanocomposites is highly reproducible. The LSPR of AuNPs (mean diameter ~ 60 nm) embedded in the polymeric networks of increasing MW exhibited different values in terms of peak position and absorbance intensity (Fig. 7a). More precisely, the P700Au with a lower SR (Fig. 6c) exhibited a $\lambda_{max} = 555.3 \pm 0.8$ nm and an absorbance intensity (located at λ_{max}) of 0.67 ± 0.03. Differently, the P2000Au nanocomposite exhibited a blueshift in the LSPR position, located at $\lambda_{max} = 551.4 \pm 0.7$ nm, and a decrease in the absorbance intensity down to 0.53 ± 0.04. Then, the P6000Au samples exhibited a further blueshift in the LSPR ($\lambda_{max} = 545.8 \pm 0.4$ nm) and a further decrease in the absorbance (0.39 ± 0.02). Finally, the P10000Au samples exhibited a redshift in the LSPR, compared to the P6000Au nanocomposites ($\lambda_{max} = 548.4 \pm 0.6$ nm) and a further decrease in the absorbance intensity (0.25 ± 0.02).

In this paper, an explanation of the different behavior of AuNPs embedded in PEGDA with increasing MW is found and directly correlated with the PEGDA refractive index (Fig. 2b) and SR (Fig. 6c). Theoretical simulations based on the application of Mie theory [33,45] to 60 nm AuNP surrounded by a dielectric medium ($n_{eff,m}$) made of water (n_{Water}) and PEGDA (n_P) with known refractive

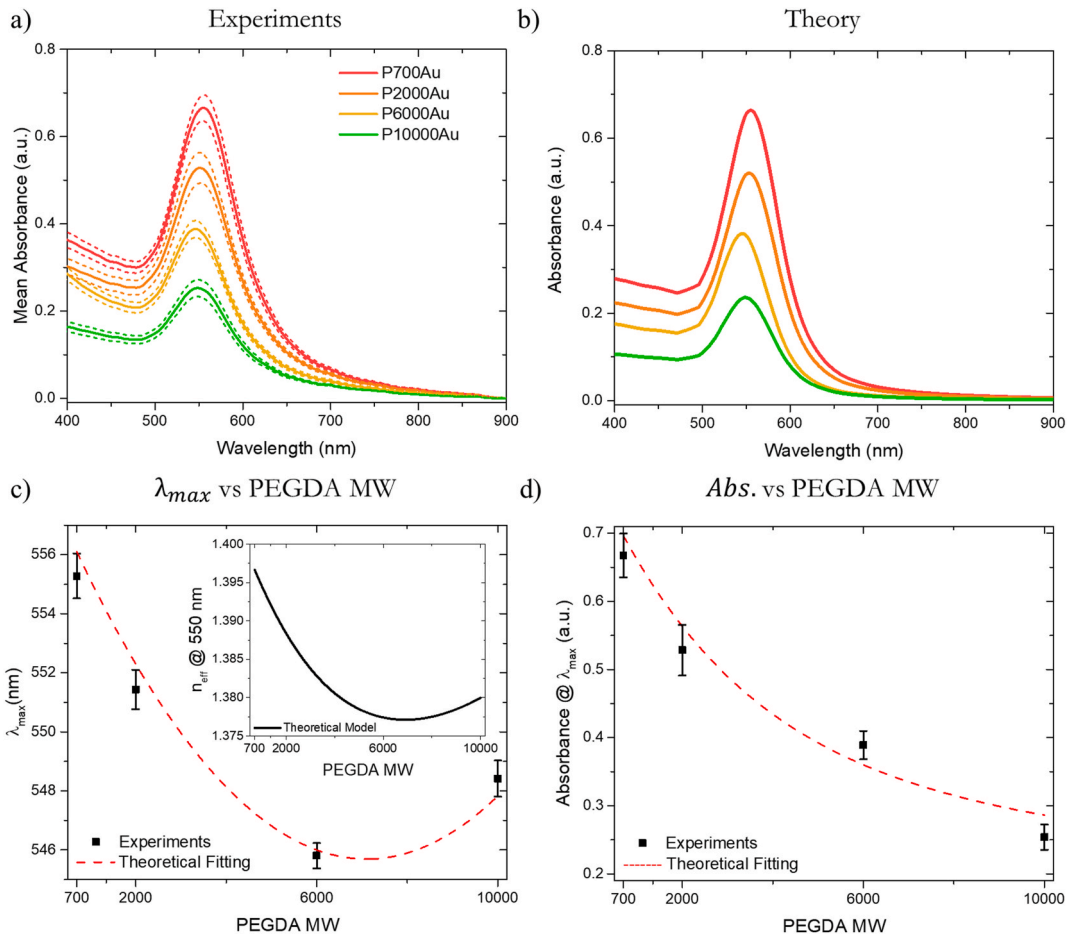

Fig. 7. a) Mean experimental absorbance spectra of P700Au, P2000Au, P6000Au, and P10000Au (solid lines). The dashed lines denote the confidence interval obtained from the average on a minimum of three independent samples ($n \geq 3$). b) Theoretical prediction of the absorption spectra of a 60 nm size AuNP embedded in media with effective refractive indexes, depending on the PEGDA and water content. c) Mean LSPR position λ_{max} as a function of the PEGDA MW and theoretical fitting (dashed red line) obtained by using the effective refractive index reported in the inset. d) Mean LSPR intensity as a function of the PEGDA MW and theoretical fitting (dashed red line) obtained by considering the SR(MW). Vertical bars are representative of the SD on three independent measurements ($n \geq 3$).

indexes were performed. The prediction of the absorption cross-section of citrate-capped AuNPs (~60 nm) was performed by GA optimization as reported in Refs. [26,34,37,38] and as explained in detail in the experimental section. However, citrate-capped AuNPs with a mean diameter of 60 nm exhibit LSPR at ~540 nm in water. Therefore, polymerized PEGDA hydrogels cause a significant redshift of the LSPR due to their refractive index, which is higher than n_{Water}, as reported in Fig. 2b. The results of the numerical simulations (Fig. 7b) were obtained by considering the polymer and water fractions, according to the measured SR. The effective refractive index of the medium surrounding the AuNPs ($n_{eff,m}$) was optimized to minimize the norm of the difference between experimental and numerical prediction. The simulations are in excellent agreement with the experimental data and allowed the formulation of a model to predict the effective refractive index of the AuNPs surroundings as a function of the PEGDA MW. The effective refractive index $n_{eff,m}$ was found to have a parabolic dependency on the MW (Fig. 7c) and was identified as in equation (7):

$$n_{eff,m}(MW) = K_f\left(\frac{1}{SR(MW)+1}n_P(MW) + \frac{SR(MW)}{SR(MW)+1}n_{water}\right) + K_b\, n_P(MW) \tag{7}$$

In Equation (5), $n_P(MW)$ is the experimentally measured refractive index as reported in Fig. 2b. At 550 nm, it is possible to find an empirical parabolic relationship between n_P and the MW (Fig. S3a) as in equation (8):

$$n_P(MW)|_{550\ nm} = A_1 \cdot MW^2 + B_1 \cdot MW + C_1 \tag{8}$$

Analogously, the SR can be expressed as a function of the MW with the following Equation (9) (Fig. S3b):

$$SR(MW) = A_2 \cdot MW^2 + B_2 \cdot MW + C_2 \tag{9}$$

The coefficients $A_{1,2}$, $B_{1,2}$, and $C_{1,2}$ are summarized in Table S1. The quantities $\frac{1}{SR(MW)+1}$ and $\frac{SR(MW)}{SR(MW)+1}$ denote the polymer and water fractions in the AuNPs surroundings, respectively. Moreover, no leakage of AuNPs is observed during the swelling of all four nanocomposites. This means that the AuNPs are physically entrapped in the polymer network, and, therefore, part of the AuNPs surface must be physically in contact (*bound*) with PEGDA molecules. This justifies the use of two weighting coefficients K_f and K_b. K_f denotes the portion of the AuNPs surface that is, on average, exposed to water and polymer, weighted as a function of the SR, while K_b denotes the portion of the AuNPs, which is strictly in contact with PEGDA. The function $n_{eff,m}(MW)$ and its subsequent application to the numerical simulations are reported in Fig. 7c. By assuming $K_f = 0.85$ and $K_b = 0.15$, an excellent agreement between theory and experiments was found. The parabolic correlation between the expected LSPR position λ_{max} as a function of the PEGDA MW well explains the experimental data and the behavior of AuNPs in the different polymeric networks.

The absorption intensity, instead, was found to simply depend on the SR(MW), reported in Equation (10) as follows:

$$C_{Abs}|_{\lambda_{max}} = \frac{1 + C_{min} \cdot SR(MW)}{SR(MW)} \tag{10}$$

where $C_{Abs}|_{\lambda_{max}}$ denotes the absorbance intensity at the LSPR wavelength, and C_{min} is the minimum recorded absorbance intensity that depends on the adopted experimental setup, the light source spot size, and on the optical density of AuNPs within the hydrogel network. In the present study, by imposing $C_{min} = 0.2$, an excellent agreement between experiments and theoretical modeling was achieved, as shown in Fig. 7d.

Therefore, the proposed optical modeling provides a complete description of the optical response of AuNPs embedded in PEGDA hydrogels of increasing MW and could be in principle adopted in the theoretical prediction of the optical behavior of any combination

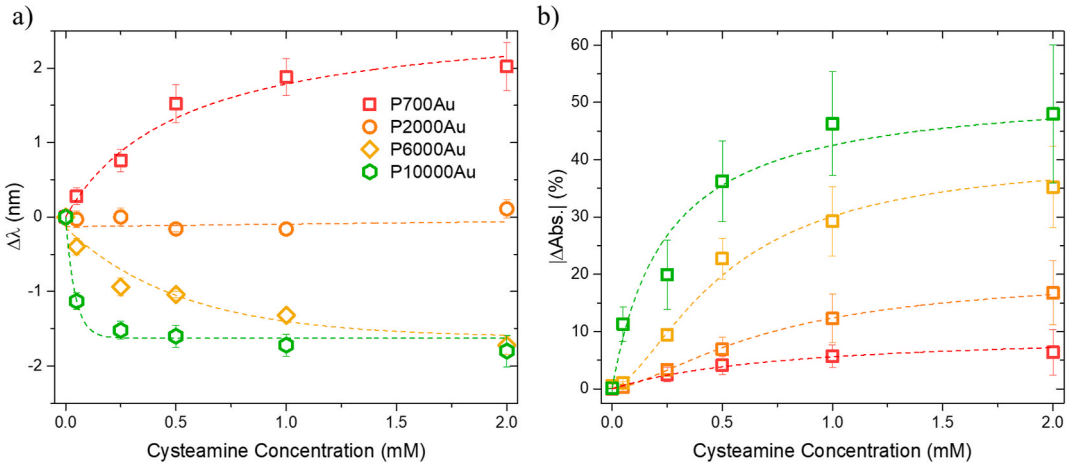

Fig. 8. (a) LSPR position variation $\Delta\lambda$ and (b) absolute value of the LSPR intensity variation $|\Delta Abs.|$ as a function of the cysteamine concentration for P700Au (red squares), P2000Au (orange circles), P6000Au (yellow rhombuses), and P10000Au (green hexagons) nanocomposites. The theoretical fittings are reported as dashed lines. The SD are reported as vertical bars ($n \geq 3$).

of hydrogels with tunable MW and plasmonic NPs.

3.6. Application in optical biosensing

In this section, we report on the promising application of the proposed nanocomposites in optical biosensing. Once the physicochemical properties of the hybrid transducers have been demonstrated, it is possible to directly apply the obtained transducers to molecular sensing. As a preliminary proof of concept to understand the behavior of the different nanocomposites as a function of the PEGDA MW, we chose a small molecule as cysteamine, whose sensing may be of interest in both healthcare and cosmetics [46]. Cysteamine is an aminothiol compound ($HS–CH_2–CH_2–NH_2$), which spontaneously forms monolayers on AuNPs thanks to thiol-Au interactions [47].

All the nanocomposites object of this study were soaked into cysteamine water solutions having different concentrations (from 50 μ M to 2.0 mM). The optical spectra were recorded, as reported in the Experimental section, and peak position (λ_{max}) and absorbance intensity at λ_{max} were analyzed. Fig. 8a and b show the variation in LSPR position ($\Delta\lambda$) and absorbance intensity ($|\Delta Abs.|$) as a function of the cysteamine concentration. Interestingly, only the P700Au nanocomposites exhibited a significant λ_{max} redshift as a function of the cysteamine concentration (highest Sensitivity and lowest LOD, as shown in Table S2). The LSPR of P2000Au samples remained mostly unchanged as a function of the cysteamine concentration. Finally, P6000Au and P10000Au nanocomposites exhibited a blueshift of the LSPR peak, as a function of the cysteamine concentration. *Vice versa*, the most significant variations in absorbance intensity were observed for P10000Au (highest sensitivity and lowest LOD, as shown in Table S2), in which, at saturation, a 50 % absorbance decrease was observed (note that $\Delta Abs.$ is reported as absolute value). The absorbance intensity of P700Au nanocomposites, instead, remained mostly unchanged as a function of the cysteamine concentration (lowest sensitivity and highest LOD, as shown in Table S2).

The different behavior of the four nanocomposites can be explained by the intrinsic extremely high hydrophilic nature of cysteamine [48]. Indeed, when it is bound to the AuNPs in the nanocomposites, it causes a significant increase in the swelling equilibrium. The increase in the swelling equilibrium is more evident in the networks with the lowest elastic moduli, namely P10000Au, while it is less significant in more rigid networks, such as P700Au. Therefore, when more water permeates the networks, the effective medium refractive index undergoes a decrease as a function of the cysteamine. The decrease of $n_{eff,m}$ counterbalances (in the case of P2000Au) or overcomes (in the case of P6000Au and P10000Au) the redshift that the cysteamine would have caused on AuNPs if they were in the water. Therefore, only for P700Au a redshift of the LSPR can be observed, since the increase of the hydrogel swelling equilibrium is not high enough to counterbalance the adsorption of cysteamine on the AuNPs surface.

To understand this behavior, we performed numerical simulations by adopting the theoretical model introduced in the previous section. More precisely, we assumed cysteamine as a layer (estimated as 5 Å thick) and we computed the theoretical absorbance spectra of AuNPs embedded in the networks with the four different MW. The obtained theoretical fitting well predicts the experimental data only if we consider the enhancement of the SR values as a function of the cysteamine concentration.

The obtained results demonstrate that low MW hydrogels (P700Au) can be used as optical transducers based on refractometric sensing, as the standard LSPR-based biosensors. Differently, high MW hydrogels (P6000Au and P10000Au), due to their mechanical properties, can give rise to new paradigms in the biosensing field. Indeed, if opportunely functionalized, the AuNPs can exhibit significant variation in their LSPR intensity as a function of a target concentration. Moreover, having a relatively bigger network mesh size, they could be easily applied also for the detection of viruses, bacteria, and cells [49].

4. Conclusions

In this paper, we proposed a comprehensive model of PEGDA/AuNPs nanocomposite transducers for biosensing applications based on their optical and physicochemical characterization. PEGDA monomers with MW of 700, 2000, 6000, and 10,000 Da were investigated embedding a monodisperse distribution of AuNPs. The chemical, thermal, and mechanical stability of these hybrid materials makes them ideal candidates for biosensing purposes. Moreover, the homogeneous and highly reproducible dispersion of AuNPs within the polymeric networks enabled the theoretical investigation of the optical properties of the AuNPs as a function of the PEGDA monomer MW. The LSPR peak position exhibited by AuNPs was found to be a parabolic function of the monomer MW, while, fixed the incident light spot, the absorbance intensity was found to decrease with the increase in the MW. All the nanocomposites were tested as biosensors of a simple, small, model molecule, the cysteamine, and due to the highly hydrophilic nature of this molecule, different behaviors of the AuNPs LSPR as a function of its concentration were found. Low MW hydrogels, with poor swelling capability were found to be highly sensitive to refractive index variations, even for a small molecule, as cysteamine. High MW hydrogels were found to have a swelling equilibrium variation, and consequently an LSPR absorbance intensity, highly sensitive to the cysteamine concentration. The obtained results were all supported by numerical simulations, which were based on the highly distributed and *non-interacting* AuNPs within the hydrogel network. We envisage that the proposed platforms could find large applications in wearable sensing, food quality control, and *in-vitro* assays for the monitoring of cell cultures.

Data availability statement

Data will be made available on request.

CRediT authorship contribution statement

Bruno Miranda: Writing – review & editing, Writing – original draft, Visualization, Validation, Software, Investigation, Formal analysis, Data curation, Conceptualization. **Stefania Dello Iacono:** Writing – review & editing, Writing – original draft, Visualization, Validation, Supervision, Project administration, Methodology, Investigation, Formal analysis, Data curation, Conceptualization. **Ilaria Rea:** Writing – review & editing, Visualization, Methodology, Formal analysis. **Fabio Borbone:** Writing – review & editing, Visualization, Methodology, Formal analysis. **Luca De Stefano:** Writing – review & editing, Visualization, Supervision, Resources, Methodology, Funding acquisition, Formal analysis, Conceptualization.

Declaration of competing interest

The authors declare that they have no known competing financial interests or personal relationships that could have appeared to influence the work reported in this paper.

Acknowledgements

Luca De Stefano acknowledges the partial financial support from CNR @Projects SAC.AD002.173.026 TIPPS (Tracking and Identification of asymptomatic Patients through engineered antibodies bioconjugated plasmonics in a Pandemic Scenario).

Appendix A. Supplementary data

Supplementary data to this article can be found online at https://doi.org/10.1016/j.heliyon.2024.e25593.

References

[1] M. Xu, D. Obodo, V.K. Yadavalli, The design, fabrication, and applications of flexible biosensing devices, Biosens. Bioelectron. 124–125 (2019) 96–114, https://doi.org/10.1016/j.bios.2018.10.019.
[2] C. Huang, K. Bonroy, G. Reekmans, W. Laureyn, K. Verhaegen, I. De Vlaminck, L. Lagae, G. Borghs, Localized surface plasmon resonance biosensor integrated with microfluidic chip, Biomed. Microdevices 11 (2009) 893–901, https://doi.org/10.1007/s10544-009-9306-8.
[3] M. Soler, C.S. Huertas, L.M. Lechuga, Label-free plasmonic biosensors for point-of-care diagnostics: a review, Expert Rev. Mol. Diagn. 19 (2019) 71–81, https://doi.org/10.1080/14737159.2019.1554435.
[4] R. Rebelo, A.I. Barbosa, D. Caballero, I.K. Kwon, J.M. Oliveira, S.C. Kundu, R.L. Reis, V.M. Correlo, 3D biosensors in advanced medical diagnostics of high mortality diseases, Biosens. Bioelectron. 130 (2019) 20–39, https://doi.org/10.1016/j.bios.2018.12.057.
[5] C. Folks, U.S. Phuyal, M. Rajesh, N. Arja, M. Gladden, L. Hamm, A.S. De Silva Indrasekara, Fabrication and comparative quantitative analysis of plasmonic-polymer nanocomposites as optical platforms, Langmuir 37 (2021) 12853–12866, https://doi.org/10.1021/ACS.LANGMUIR.1C01826/SUPPL_FILE/LA1C01826_SI_001.PDF.
[6] S.I. Lepeshov, A.E. Krasnok, P.A. Belov, A.E. Miroshnichenko, Hybrid Nanophotonics, Uspekhi Fiz. Nauk, 2018, pp. 1137–1154, https://doi.org/10.3367/ufnr.2017.12.038275.
[7] C.I.L. Justino, A.C. Duarte, T.A.P. Rocha-Santos, Recent progress in biosensors for environmental monitoring: a review, Sensors (Switzerland) 17 (2017), https://doi.org/10.3390/s17122918.
[8] M. Nehra, Kanika, N. Dilbaghi, R. Kumar, S. Kumar, Trends in point-of-care optical biosensors for antibiotics detection in aqueous media, Mater. Lett. 308 (2022) 131235, https://doi.org/10.1016/J.MATLET.2021.131235.
[9] Y. Ning, G.Q. Jin, M.X. Wang, S. Gao, J.L. Zhang, Recent progress in metal-based molecular probes for optical bioimaging and biosensing, Curr. Opin. Chem. Biol. 66 (2022) 102097, https://doi.org/10.1016/J.CBPA.2021.102097.
[10] B. Kaur, S. Kumar, B.K. Kaushik, Recent advancements in optical biosensors for cancer detection, Biosens. Bioelectron. 197 (2022) 113805, https://doi.org/10.1016/J.BIOS.2021.113805.
[11] Z.L. Lei, B. Guo, 2D material-based optical biosensor: status and prospect, Adv. Sci. 9 (2022) 2102924, https://doi.org/10.1002/ADVS.202102924.
[12] B. Miranda, I. Rea, P. Dardano, L. De Stefano, C. Forestiere, Recent advances in the fabrication and functionalization of flexible optical biosensors: toward smart life-sciences applications, Biosensors 11 (2021) 107, https://doi.org/10.3390/bios11040107.
[13] V. Nocerino, B. Miranda, C. Tramontano, G. Chianese, P. Dardano, I. Rea, L. De Stefano, Plasmonic nanosensors: design, fabrication, and applications in biomedicine, Chemosens 10 (2022) 150, https://doi.org/10.3390/CHEMOSENSORS10050150.
[14] S. Unser, I. Bruzas, J. He, L. Sagle, Localized surface plasmon resonance biosensing: current challenges and approaches, Sensors 15 (2015) 15684–15716, https://doi.org/10.3390/s150715684.
[15] H. Sun, H. Liu, Y. Wu, A green, reusable SERS film with high sensitivity for in-situ detection of thiram in apple juice, Appl. Surf. Sci. 416 (2017) 704–709, https://doi.org/10.1016/j.apsusc.2017.04.159.
[16] D. Shir, Z.S. Ballard, A. Ozcan, Flexible plasmonic sensors, IEEE J. Sel. Top. Quant. Electron. 22 (2016) 12–20, https://doi.org/10.1109/JSTQE.2015.2507363.
[17] X. Lin, W.L.J. Hasi, S.Q.G.W. Han, X.T. Lou, D.Y. Lin, Z.W. Lu, Fabrication of transparent SERS platform via interface self-assembly of gold nanorods and gel trapping technique for on-site real time detection, Phys. Chem. Chem. Phys. 17 (2015) 31324–31331, https://doi.org/10.1039/c5cp04828a.
[18] L. Li, W.S. Chin, Rapid fabrication of a flexible and transparent Ag nanocubes@PDMS film as a SERS substrate with high performance, ACS Appl. Mater. Interfaces 12 (2020) 37538–37548, https://doi.org/10.1021/acsami.0c07178.
[19] Y.S. Zhang, A. Khademhosseini, Advances in engineering hydrogels, Science (80-.) 356 (2017), https://doi.org/10.1126/SCIENCE.AAF3627/ASSET/FF981CF9-F818-45D8-A693-CA10D4ABEE12/ASSETS/GRAPHIC/356_AAF3627_F5.
[20] I. Willner, Stimuli-controlled hydrogels and their applications, Acc. Chem. Res. 50 (2017) 657–658, https://doi.org/10.1021/ACS.ACCOUNTS.7B00142.
[21] Q. Shi, H. Xia, P. Li, Y.-S. Wang, L. Wang, S.-X. Li, G. Wang, C. Lv, L.-G. Niu, H.-B. Sun, Q. Shi, H. Xia, P. Li, Y. Wang, L. Wang, S. Li, G. Wang, C. Lv, L. Niu, H. Sun, Photothermal surface plasmon resonance and interband transition-enhanced nanocomposite hydrogel actuators with hand-like dynamic manipulation, Adv. Opt. Mater. 5 (2017) 1700442, https://doi.org/10.1002/ADOM.201700442.
[22] M. Battisti, S. De Martino, B. Miranda, C. Tammaro, P. Dardano, S. Dello Iacono, A. Luca, D.E. Stefano, Oxygen indicator films of acrylate photopolymers and TiO 2 nanoparticles with tunable response times, Opt. Mater. Express 11 (2021) 2244, https://doi.org/10.1364/OME.426500.

[23] M. Mesch, C. Zhang, P.V. Braun, H. Giessen, Functionalized hydrogel on plasmonic nanoantennas for noninvasive glucose sensing, ACS Photonics 2 (2015) 475–480, https://doi.org/10.1021/ACSPHOTONICS.5B00004/ASSET/IMAGES/LARGE/PH-2015-00004N_0005.
[24] I.B. Ansah, S. Kim, J.-Y. Yang, C. Mun, H.S. Jung, S. Lee, D.-H. Kim, S.-H. Kim, S.-G. Park, I.B. Ansah, J.-Y. Yang, C. Mun, H.S. Jung, S. Lee, D.-H. Kim, S.-G. Park, S. Kim, S.-H. Kim, In situ electrodeposition of gold nanostructures in 3D ultra-thin hydrogel skins for direct molecular detection in complex mixtures with high sensitivity, Laser Photon. Rev. 15 (2021) 2100316, https://doi.org/10.1002/LPOR.202100316.
[25] A. Choe, J. Yeom, R. Shanker, M.P. Kim, S. Kang, H. Ko, Stretchable and wearable colorimetric patches based on thermoresponsive plasmonic microgels embedded in a hydrogel film, NPG Asia Mater. 10 (2018) 912–922, https://doi.org/10.1038/s41427-018-0086-6.
[26] B. Miranda, R. Moretta, S. De Martino, P. Dardano, I. Rea, C. Forestiere, L. De Stefano, A PEGDA hydrogel nanocomposite to improve gold nanoparticles stability for novel plasmonic sensing platforms, J. Appl. Phys. 129 (2021) 033101, https://doi.org/10.1063/5.0033520.
[27] B. Miranda, R. Moretta, P. Dardano, I. Rea, C. Forestiere, L. De Stefano, H3 (Hydrogel-Based, high-sensitivity, hybrid) plasmonic transducers for biomolecular interactions monitoring, Adv. Mater. Technol. (2022) 2101425, https://doi.org/10.1002/ADMT.202101425.
[28] D. Yilmaz, B. Miranda, E. Lonardo, I. Rea, L. De Stefano, A.C. De Luca, SERS-based pH-Dependent detection of sulfites in wine by hydrogel nanocomposites, Biosens. Bioelectron. 245 (2024) 115836, https://doi.org/10.1016/j.bios.2023.115836.
[29] P. Kanmani, J.W. Rhim, Physicochemical properties of gelatin/silver nanoparticle antimicrobial composite films, Food Chem. 148 (2014) 162–169, https://doi.org/10.1016/J.FOODCHEM.2013.10.047.
[30] N.G. Bastús, J. Comenge, V. Puntes, Kinetically controlled seeded growth synthesis of citrate-stabilized gold nanoparticles of up to 200 nm: size focusing versus ostwald ripening, Langmuir 27 (2011) 11098–11105, https://doi.org/10.1021/la201938u.
[31] H. Zhang, L. Wang, L. Song, G. Niu, H. Cao, G. Wang, H. Yang, S. Zhu, Controllable properties and microstructure of hydrogels based on crosslinked poly (ethylene glycol) diacrylates with different molecular weights, J. Appl. Polym. Sci. 121 (2011) 531–540, https://doi.org/10.1002/APP.33653.
[32] W. Sellmeier, Ueber die durch die Aetherschwingungen erregten Mitschwingungen der Körpertheilchen und deren Rückwirkung auf die ersteren, besonders zur Erklärung der Dispersion und ihrer Anomalien, Ann. Phys. 223 (1872) 386–403, https://doi.org/10.1002/ANDP.18722231105.
[33] T. Wriedt, Mie theory: a review, Springer Opt. Sci. 169 (2012) 53–71, https://doi.org/10.1007/978-3-642-28738-1_2.
[34] C. Forestiere, A.J. Pasquale, A. Capretti, G. Miano, A. Tamburrino, S.Y. Lee, B.M. Reinhard, L. Dal Negro, Genetically engineered plasmonic nanoarrays, Nano Lett. 12 (2012) 2037–2044, https://doi.org/10.1021/nl300140g.
[35] L. Wang, M.H. Kafshgari, M. Meunier, Optical properties and applications of plasmonic-metal nanoparticles, Adv. Funct. Mater. 30 (2020) 2005400, https://doi.org/10.1002/ADFM.202005400.
[36] S.A. Maier, Plasmonics: Fundamentals and Applications, 2007. https://books.google.it/books?hl=it&lr=&id=yT2ux7TmDc8C&oi=fnd&pg=PR7&dq=plasmonics+fundamentals+and+applications&ots=ugu66s2M3u&sig=iYSyOz3Kjzu_R34y0unvVTF-yQk#v=onepage&q=plasmonics fundamentals and applications&f=false. (Accessed 22 February 2021).
[37] C. Tramontano, B. Miranda, G. Chianese, L. De Stefano, C. Forestiere, M. Pirozzi, I. Rea, Design of gelatin-capped plasmonic-diatomite nanoparticles with enhanced galunisertib loading capacity for drug delivery applications, Int. J. Mol. Sci. 22 (2021), https://doi.org/10.3390/ijms221910755.
[38] R.L. Haupt, D.H. Werner, Genetic Algorithms in Electromagnetics, John Wiley and Sons, Hoboken, New Jersey, 2006, https://doi.org/10.1002/047010628X.
[39] P.B. Johnson, R.W. Christy, Optical constants of the noble metals, Phys. Rev. B 6 (1972) 4370–4379, https://doi.org/10.1103/PhysRevB.6.4370.
[40] V.A. Markel, Introduction to the Maxwell garnett approximation: tutorial, J. Opt. Soc. Am. A 33 (2016) 1244, https://doi.org/10.1364/josaa.33.001244.
[41] Y. Battie, A. Resano-Garcia, N. Chaoui, Y. Zhang, A. En Naciri, Extended Maxwell-Garnett-Mie formulation applied to size dispersion of metallic nanoparticles embedded in host liquid matrix, J. Chem. Phys. 140 (2014), https://doi.org/10.1063/1.4862995.
[42] I. Pastoriza-Santos, C. Kinnear, J. Pérez-Juste, P. Mulvaney, L.M. Liz-Marzán, Plasmonic polymer nanocomposites, Nat. Rev. Mater. 310 (3) (2018) 375–391, https://doi.org/10.1038/s41578-018-0050-7.
[43] P. Dardano, S. De Martino, M. Battisti, B. Miranda, I. Rea, L. De Stefano, One-shot fabrication of polymeric hollow microneedles by standard photolithography, Polymers 13 (2021) 520, https://doi.org/10.3390/polym13040520.
[44] B. Miranda, M. Battisti, S. De Martino, V. Nocerino, P. Dardano, L. De Stefano, G. Cangiano, Hollow microneedle-based plasmonic sensor for on patch detection of molecules in dermal interstitial fluid, Adv. Mater. Technol. (2023) 1–15, https://doi.org/10.1002/admt.202300037, 2300037.
[45] Q. Fu, W. Sun, Mie theory for light scattering by a spherical particle in an absorbing medium, Appl. Opt. 40 (2001) 1354, https://doi.org/10.1364/ao.40.001354.
[46] T.C. Pham, S. Lee, Y.R. Son, M. Kwak, H.S. Kim, S. Lee, Simultaneous and visual detection of cysteamine based on Michael addition reaction with polydiacetylene liposomes †, J. Mater. Chem. C 8 (2020) 15290 https://doi.org/10.1039/d0tc02721a.
[47] M. Wirde, U. Gelius, L. Nyholm, Self-assembled monolayers of cystamine and cysteamine on gold studied by XPS and voltammetry, Langmuir 15 (1999) 6370–6378, https://doi.org/10.1021/la9903245.
[48] S. Pescina, F. Carra, C. Padula, P. Santi, S. Nicoli, Effect of pH and penetration enhancers on cysteamine stability and trans-corneal transport, Eur. J. Pharm. Biopharm. 107 (2016) 171–179, https://doi.org/10.1016/j.ejpb.2016.07.009.
[49] R. Randriantsilefisoa, C. Nie, B. Parshad, Y. Pan, S. Bhatia, R. Haag, Double trouble for viruses: a hydrogel nanocomposite catches the influenza virus while shrinking and changing color, Chem. Commun. 56 (2020) 3547–3550, https://doi.org/10.1039/c9cc09069j.